CIRP Annals - Manufacturing Technology 71 (2022) 281–284

Contents lists available at ScienceDirect

CIRP Annals - Manufacturing Technology

journal homepage: https://www.editorialmanager.com/CIRP/default.aspx

Surface integrity in high-speed grinding of Al6061T6 alloy

Sai Guo[a,b], Jianqiu Zhang[a], Qinghong Jiang[a], Bi Zhang (1)[a,*]

[a] Shenzhen Key Laboratory of Cross-Scale Manufacturing Mechanics, Southern University of Science and Technology, Shenzhen 518055, China
[b] State Key Laboratory of Ultraprecision Machining Technology, Department of Industrial and Systems Engineering, The Hong Kong Polytechnic University, Kowloon, Hong Kong, China

ARTICLE INFO

Article history:
Available online 1 April 2022

Keywords:
Surface integrity
Grinding
Damage skin effect

ABSTRACT

High-ductility materials often impose grinding problems. This study carries out high-speed grinding on the Al6061T6 alloy at a linear grinding speed of 30.4–307.0 m/s to explore surface integrity and material removal mechanisms from the perspectives of material embrittlement and damage skin effect. The results reveal that the micrograins are refined into the equiaxed nanograins in the Al6061T6 workpieces subjected to grinding. Continuous dynamic recrystallization is induced at a decreasing depth with an increasing grinding speed due to the high strain-rate field and the reduced depth of the heat affected layer, manifesting a result of damage skin effect.

1. Introduction

The mechanical properties of a ductile material can drastically increase in its strength and hardness, but decrease in its fracture toughness when the material is subjected to a high strain-rate deformation process, resulting in material embrittlement [1,2]. In the high strain-rate deformation process, dislocations may pile-up to form energy barriers [2]. High strain-rate not only results in material embrittlement, but also the skin effect of machining-induced damage [3].

As a metallic material with high specific strength and heat treatability, aluminum alloy 6061 (Al6061T6) is widely used for structural applications in aerospace, marine, and automotive industries [4]. However, Al6061T6 is difficult-to-grind due to its high ductility which often creates grinding problems, such as poor surface integrity and dimensional accuracies, as well as severe wheel wear [4,5]. Strain-rate evoked material embrittlement paves a practical way towards grinding materials with high efficiency and high quality [2]. In high-speed grinding (HSG) of high-ductility materials (e.g., Al6061T6), the problems, such as high wheel loading and severe workpiece burn, will no longer exist because heat generation can markedly be suppressed due to the effect of material embrittlement. Moreover, grinding-induced material deformation is confined in a superficial layer of the ground surface on account of the damage skin effect.

Although other scholars have carried out extensive studies on deformation and fracture behaviors of aluminum alloys in high-speed machining [4–7], few studies were conducted to comprehensively investigate the surface integrity of a ground workpiece from the perspectives of material embrittlement and damage skin effect. To explore surface integrity and material removal mechanisms of the Al6061T6 alloy under high strain-rates, this study carries out HSG at a linear grinding speed ranging from 30.4 m/s to 307.0 m/s, and performs extensive investigations on surface integrity of the ground workpieces. Moreover, finite element modeling (FEM) of the HSG process is also conducted to facilitate understanding of the subsurface formation during the process.

2. Experimental details

Commercially available wrought Al6061T6 (Goodfellow Cambridge Ltd., UK) was chosen as the workpiece material. Prior to the grinding experiments, the Al6061T6 was cut and polished into workpieces with dimensions of 10.0 × 10.0 × 3.0 mm. In this study, HSG of the Al6061T6 workpieces was carried out on a grinding machine (Quest GT27, Hardinge, USA) which was equipped with a customized high-speed hydrostatic motorized spindle (TDM SA, Switzerland), as shown in Fig. 1. The high stiffness and high rotational accuracy of the spindles guaranteed high geometrical accuracy and good surface finish. The grinding wheel for HSG had a substrate made up with carbon fiber reinforced plastics (CFRP), and a vitrified bonded CBN abrasive

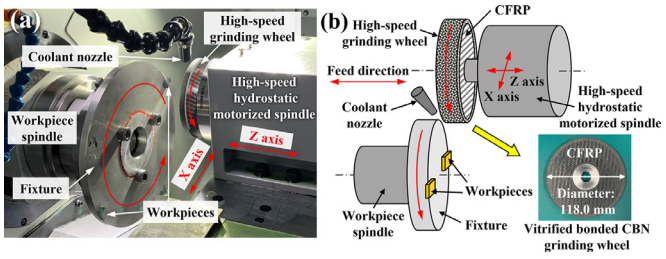

Fig. 1. (a) Experimental setup and (b) schematic diagram for HSG arrangement of the Al6061T6 workpieces.

* Corresponding author.
E-mail address: zhangb@sustech.edu.cn (B. Zhang).

https://doi.org/10.1016/j.cirp.2022.03.002

layer with a wheel concentration of 175%. The grinding wheel had a diameter of 118.0 mm, thickness of 10.0 mm, and mesh size of #120.

Prior to each grinding trial, the grinding wheel was first trued using a diamond rolling wheel and sharpened by a SiC grinding wheel in advance, and then balanced using a dynamic balancing instrument (BMT240M.2, MPM, Germany). HSG was performed according to the parameters tabulated in Table 1 where six trials were designed to investigate the effect of grinding speed ranging from 30.4 m/s to 307.0 m/s on the surface integrity of the Al6061T6 workpieces. During the grinding experiment, flood cooling was employed to cool and reduce friction in the grinding zone. For achieving a high reliability of the experimental results, triple replicated experiments for each trial were performed to obtain the average values.

Table 1
Parameters for the HSG processes of the Al6061T6 workpieces.

Trials	1	2	3	4	5	6
Wheel rotational speed n_s (rpm)	3,310	6,613	10,012	19,993	32,996	40,002
Wheel linear speed v_s (m/s)	20.4	40.8	61.8	123.5	203.8	247.0
Workpiece rotational speed n_w (rpm)	1,000	1,000	1,000	1,000	1,000	6,000
Workpiece linear speed v_w (m/s)	10	10	10	10	10	60
Grinding depth a_p (μm)	2.5	2.5	2.5	2.5	2.5	2.5
Axial feed rate v_f (mm/min)	100	100	100	100	100	100
Grinding speed v_g (m/s)	30.4	50.8	71.8	133.5	213.8	307.0

Surface morphology of a ground workpiece was observed using a scanning electron microscope (SEM, Merlin, Zeiss, Germany). The surface three-dimensional topography was obtained by using a white light interferometer (Taylor Hobson Talysurf CCI, USA). The hardness of the ground workpieces was evaluated by a Vickers hardness tester with a load of 0.05 gf and a dwell time of 10 s. The focused ion beam (FIB) *in-situ* etching was performed on Helios Nanolab 600i (FEI, USA) to expose the cross-section along the grinding direction. The cross-sectional lamellae were prepared using the FIB milling and investigated by a transmission electron microscope (TEM, Talos F200X G2, FEI, USA).

3. Results

3.1. Ground surface morphology and surface hardness

Fig. 2(a) presents that the surface morphology of the ground workpieces differs at different grinding speeds. Before the grinding speed reached 133.5 m/s, the scale-like microtexture was the principal surface feature due to heavy surface smearing. When at $v_g \geq 133.5$ m/s, the scale-like microtexture became inconspicuous, whereas distinct grinding streaks emerged because of the relented surface plastic deformation at higher grinding speeds.

Fig. 2(b) shows the variation of surface hardness after grinding at different speeds. It is revealed that the surface hardness steadily decreased with grinding speed. It is worth noting that the workpiece after grinding at v_g = 307.0 m/s still had a surface hardness higher than that of the as-polished counterpart.

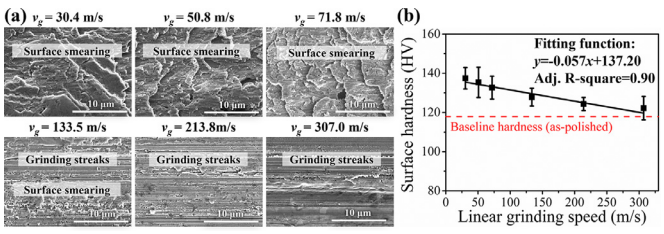

Fig. 2. (a) Surface morphology and (b) surface hardness of the Al6061T6 workpieces at different grinding speeds.

3.2. Ground surface roughness

Fig. 3(a) depicts that surface smearing with distinct bulges was identified when at v_g < 133.5 m/s, whereas grinding streaks became the dominant features with a further increase in grinding speed. As revealed in Fig. 3(b), with an increase in grinding speed, Sa and Sz sharply declined to a valley at v_g = 133.5 m/s due to the mitigated surface smearing, then gradually increased because of the surface material embrittlement at higher grinding speeds.

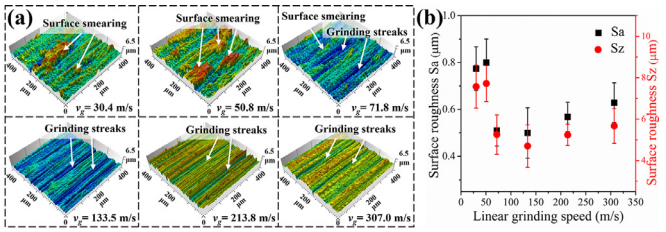

Fig. 3. (a) Surface topography and (b) surface roughness after grinding.

3.3. Grinding induced subsurface damage

Fig. 4 shows the cross-sectional views of the workpieces ground at different speeds. Two distinct regimes were identified with a well-defined boundary in the subsurface, as shown in Fig. 4(a). The topmost regime featuring severely refined equiaxed grains was the dynamic recrystallization zone (DRXZ) induced by intense plastic deformation, which was similar to that revealed in the machining of nickel-based alloys [8,9]. The DRXZ is a type of machining damage because it deteriorates the material mechanical performance with lower plasticity than the bulk material [10]. Below the DRXZ was the plastic deformation zone (PDZ), in which dynamic recrystallization (DRX) was weakened and the grains size transformed from the equiaxed nanocrystalline to the elongated microcrystalline with the evidently coarser grains. As presented in Fig. 4(b), the depth of DRXZ significantly decreased by 81.0% from ~ 2.1 μm at v_g = 30.4 m/s to ~ 0.4 μm at v_g = 307.0 m/s, manifesting an evident result of damage skin effect. Since the surface hardness was heavily influenced by the subsurface microstructure, the increased surface hardness of the workpieces after grinding was attributed to the 'Hall-Petch strengthening' effect with refined nanograins in the DRXZ [11]. However, the decreased surface hardness at an increased grinding speed resulted from the reduced depth of the DRXZ.

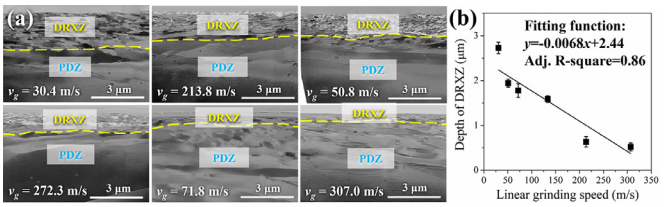

Fig. 4. (a) Subsurface microstructure of the Al6061T6 workpieces after the FIB milling; (b) the corresponding depth of the DRXZ.

As shown in Fig. 5, the morphology of the refined grains in the DRXZ is identified with a grain size smaller than 0.5 μm. Fig. 5(c) and (g) shows the selected area electron diffraction (SAED) patterns in the DRXZ, which displayed distinct polycrystalline structures. The SAED results of an equiaxed nanograin in the DRXZ of Fig. 5(a) and (e) both revealed the pristine FCC Al, as shown in Fig. 5(d) and (h), respectively, implying that no crystalline phase transformation should occur during the grinding process. As a consequence, only the grain size was refined after recrystallization, without any change in the material lattice structure.

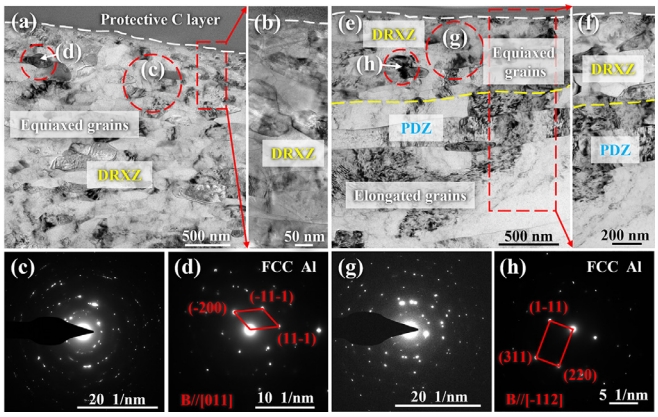

Fig. 5. TEM images and SAED patterns of the subsurfaces after grinding at v_g = 30.4 m/s (a–d) and v_g = 307.0 m/s (e–h).

Fig. 6 shows the high-angle annular dark-field (HAADF) images of the lamellar specimens to quantify the grain size of the workpieces along the depth direction from the ground surface. It was revealed in Fig. 6(a) and (b) that an oxide layer was identified in the topmost area of the DRXZ, which was resulted from the chemical reaction with oxygen in the air due to the grinding heat. It was worth noting that the depth of the oxide layer drastically dropped by 85.7% from ~ 350 nm at v_g = 30.4 m/s to ~ 50 nm at v_g = 307.0 m/s, indicating that the grinding heat was suppressed in HSG. More interestingly, the grain size gradually increased along the depth direction from the ground surface, and the grain sizes of the workpiece after grinding at v_g = 30.4 m/s were significantly smaller than those at v_g = 307.0 m/s, as shown in Fig. 6(c), indicating the evident grain refinement.

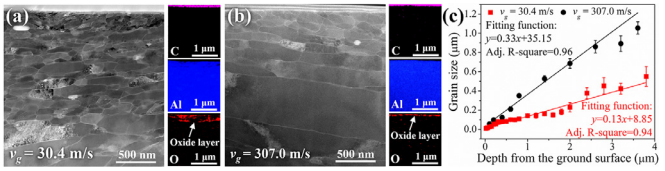

Fig. 6. Typical HAADF images of the subsurfaces after grinding at (a) v_g = 30.4 m/s, and (b) v_g = 307.0 m/s; (c) comparison of the corresponding grain size along the depth direction from the ground surface.

4. FEM of grinding temperature, strain, and strain-rate fields

To investigate the mechanisms of dynamic recrystallization in Al6061T6 below the ground surfaces, the grinding temperature, strain, and strain-rate fields should be obtained. Therefore, a single-grit grinding FEM was established with ABAQUS using the 4-node plane-strain coupled temperature-displacement elements (CPE4RT). The friction coefficient between the grit and workpiece surface was 0.5. No cooling was considered in the FEM. The element deletion technique was used to allow element separation to form chip. The model was established based on the Johnson-Cook material constitutive model [12,13],

$$\sigma = [A + B\varepsilon^n]\left[1 + Cln\left(\frac{\dot{\varepsilon}}{\dot{\varepsilon}_0}\right)\right]\left[1 - \left(\frac{T - T_r}{T_m - T_r}\right)^m\right] \quad (1)$$

where σ is the flow stress; ε represents the plastic strain; $\dot{\varepsilon}$ refers to the plastic strain-rate; $\dot{\varepsilon}_0$ is the reference strain-rate; T_r represents room temperature; and T_m refers to the melting point. Table 2 lists the optimized material parameters for the Johnson-Cook model. These parameters were determined by the perforation experiments in the speed range of 50–200 m/s [7], which roughly covered the first five grinding speeds in Table 1. Hence, the FEM in this study covered a grinding speed from 30.4 m/s to 213.8 m/s at a grinding depth of 2.5 μm.

The shear failure criterion based on the Johnson-Cook model is written as [14],

Table 2
Material parameters for the Johnson-Cook model [5].

A (MPa)	B (MPa)	C	m	n	$\dot{\varepsilon}_0$ (s^{-1})	T_r (K)	T_m (K)
201.55	250.87	0.206	1.310	0.206	0.001	293	855

$$\varepsilon_f = [D_1 + D_2 exp(D_3\sigma^*)](1 + D_4 ln\dot{\varepsilon}^*)(1 + D_5 T^*) \quad (2)$$

where D_1, D_2, D_3, D_4, and D_5 are the corresponding material parameters; σ^* is the dimensionless stress; $\dot{\varepsilon}^*$ represents the dimensionless plastic strain-rate, and T^* is the dimensionless temperature. The specific values of the material parameters are shown in Table 3.

Table 3
Johnson-Cook failure model material parameters [15].

D_1	D_2	D_3	D_4	D_5
0.0164	2.245	-2.798	0.007	3.650

5. Discussion

Based on the FEM, the variation of the strain field in the workpiece below the grit at v_g = 133.5 m/s is revealed in Fig. 7. It is found that when the grit approaches the measurement path, the measured surface strain soars up due to the increased plastic deformation. Two moments t_1 = 1.6 × 10^{-8} s and t_2 = 1.9 × 10^{-8} s in Fig. 7(a) are exploited to compare the strain field below the ground surface, as shown in Fig. 7(b) and (c), which reveal that the strain drastically decreases along the depth direction from the ground surface.

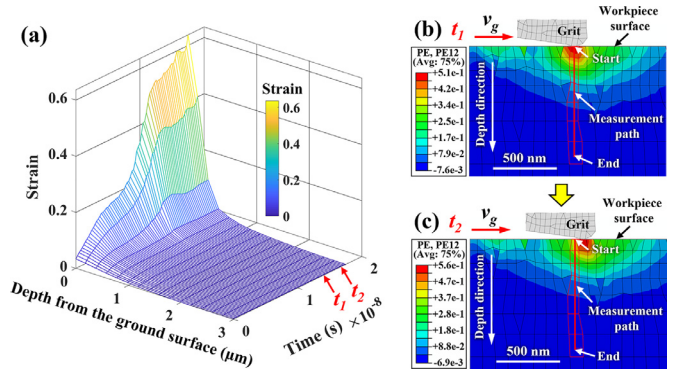

Fig. 7. (a) Variation of the strain field in the workpiece and the strain field below the grit at moment (b) t_1 and (c) t_2 at v_g = 133.5 m/s.

Fig. 8(a) and (b) depicts that the temperature and strain-rate distributions rapidly decrease along the depth direction in the ground surface when grinding at 30.4 m/s to 213.8 m/s. It is worth noting that the strain-rate fluctuates around zero as shown in Fig. 8(a) due to the severe plastic deformation. As presented in the inset of Fig. 8 (a), the subsurface regime subjected to a high strain-rate of over 1 × 10^3 s^{-1} is identified even at a depth of 2.5 μm, indicating a high-strain-rate affected regime with a depth comparable to that of the DRXZ revealed in Fig. 4. Fig. 8(b) reveals that the maximum temperature linearly increases with grinding speed. Moreover, a distinct rise of temperature gradient is identified along the depth direction from the ground surface. For instance, the depth of the regime with a temperature higher than T at an increased grinding speed is smaller compared with that produced at a lower grinding speed, indicating a reduced depth of high-temperature layer in the subsurface. Hence, it implies that an increased grinding speed induces a high temperature gradient confined in the superficial subsurface, reflecting a reduced depth of high-temperature layer. In addition, the reduced depth of oxide layer as shown in Fig. 6 also verifies the reduced depth of high-temperature layer.

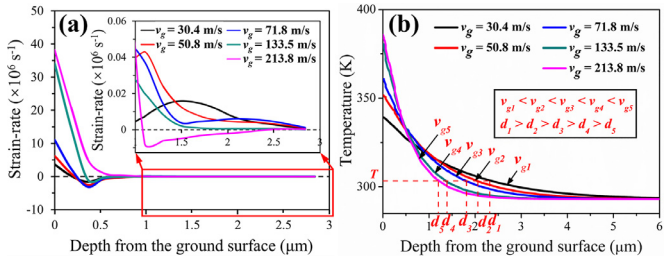

Fig. 8. (a) Strain-rate and (b) temperature distributions along the depth direction from the ground surface based on the FEM analysis.

According to Fig. 8(b), the highest temperature in the grinding regime at all the grinding speeds is below $0.5T_m$ of the Al6061T6. Beside, the flood cooling employed in the HSG further moderates the temperature rise. As a result, the maximum temperature within the deformation regime is unlikely to surpass $0.5T_m$ that is considered as the threshold temperature activating nucleation and growth based on the mechanism of the discontinuous DRX (dDRX). Therefore, the mechanism governing the grain refinement occurring below the ground surface in HSG can be considered as a high strain-induced continuous reaction, which is thus referred to as the continuous DRX (cDRX) [16].

In HSG, the cDRX refinement can occur when the workpiece material reaches the critical deformation amount. As the schematic shown in Fig. 9, the temperature, strain, and strain-rate in the workpiece material gradually decline along the depth direction from the ground surface. In the regime far below the ground surface, the pristine grains are elongated along the grinding direction and form subgrains due to a relatively low strain-rate. However, since the workpiece surface is deformed during HSG at a higher strain-rate, the new equiaxed nanograins homogeneously evolve from the subgrains. Therefore, two distinct deformation regimes form below the ground surface, i.e., the DRXZ featuring equiaxed recrystallized grains located at the topmost part of the subsurface following the mechanism of cDRX, and the PDZ with the elongated grains down below.

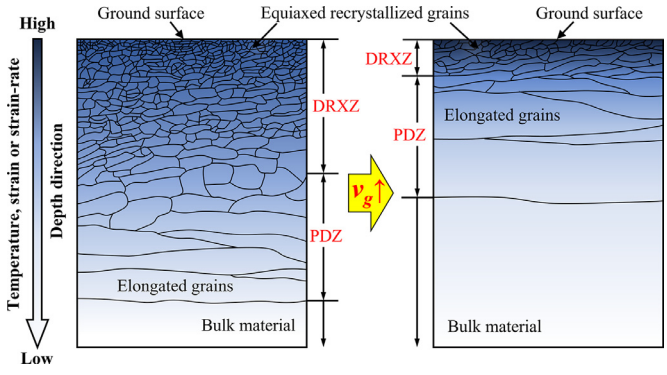

Fig. 9. Schematic of subsurface microstructural variation with grinding speed.

As the grinding speed further increases, although the surface temperature and strain-rate further increase, the temperature field that is below $0.5T_m$ is confined in the subsurface due to the reduced depth of the heat affected layer compared with that at a lower grinding speed. Hence, higher strain-rate field plays a vital role governing the subsurface formation abided by the mechanism of cDRX. Additionally, the reduced unabiding duration of grinding process further prevents the superficial plastic deformation from reaching deeper below the ground surface. As a result, these factors collectively induce the reduced depth of DRXZ, reflecting a result of damage skin effect in HSG.

6. Conclusions

For addressing the grinding problems of Al6061T6 due to its high ductility, this study carries out HSG on the Al6061T6 to explore surface integrity and material removal mechanisms under high strain-rate conditions. It reveals that surface morphology can vary from surface smearing to grinding streaks, reflecting a result of material embrittlement with the mitigated surface plastic deformation. The refined equiaxed nanograins in the ground subsurface is ascribed to the mechanism of cDRX. In addition, the decreased depth of DRXZ with an increase in the grinding speed is attributed to the high strain-rate field and the reduced depth of the heat affected layer below the ground surface, indicating a result of damage skin effect. The results imply that better surface integrity with less subsurface damage can be attained through HSG.

Declaration of Competing Interest

The authors declare that they have no known competing financial interests or personal relationships that could have appeared to influence the work reported in this paper.

Acknowledgements

This work is supported by Shenzhen Science and Technology Innovation Commission under KQTD20190929172505711 and by Shenzhen Key Laboratory of Cross-Scale Manufacturing Mechanics of Southern University of Science and Technology under ZDSYS20200810171201007.

Supplementary materials

Supplementary material associated with this article can be found in the online version at doi:10.1016/j.cirp.2022.03.002.

References

[1] Clifton RJ (2000) Response Of Materials Under Dynamic Loading. *International Journal of Solids and Structures* 37(1):105–113.
[2] Yang X, Zhang B (2019) Material Embrittlement In High Strain-Rate Loadings. *International Journal of Extreme Manufacturing* 1(2):022003.
[3] Zhang B, Yin J (2019) The 'Skin Effect' Of Subsurface Damage Distribution in Materials Subjected to High-Speed Machining. *International Journal of Extreme Manufacturing* 1(1):012007.
[4] Wang S, Xia S, Wang H, Yin Z, Sun Z (2020) Prediction of Surface Roughness in Diamond Turning of Al6061 With Precipitation Effect. *Journal of Manufacturing Processes* 60:292–298.
[5] Scapin M, Manes A (2018) Behaviour Of Al6061-T6 Alloy At Different Temperatures And Strain-Rates: Experimental Characterization And Material Modelling. *Materials Science and Engineering: A* 734:318–328.
[6] Shimizu J, Zhou LB, Eda H (2002) Simulation And Experimental Analysis Of Super High-Speed Grinding Of Ductile Material. *Journal of Materials Processing Technology* 129(1):19–24.
[7] Rodríguez-Millán M, Vaz-Romero A, Rusinek A, Rodríguez-Martínez JA, Arias A (2014) Experimental Study on the Perforation Process Of 5754-H111 and 6082-T6 Aluminium Plates Subjected to Normal Impact by Conical, Hemispherical and Blunt Projectiles. *Experimental Mechanics* 54(5):729–742.
[8] M'Saoubi R, Axinte D, Herbert C, Hardy M, Salmon P (2014) Surface Integrity of Nickel-Based Alloys Subjected to Severe Plastic Deformation by Abusive Drilling. *CIRP Annals* 63(1):61–64.
[9] M'Saoubi R, Larsson T, Outeiro J, Guo Y, Suslov S, Saldana C, Chandrasekar S (2012) Surface Integrity Analysis of Machined Inconel 718 Over Multiple Length Scales. *CIRP Annals* 61(1):99–102.
[10] Liao Z, Polyakov M, Diaz OG, Axinte D, Mohanty G, Maeder X, Michler J, Hardy M (2019) Grain Refinement Mechanism of Nickel-Based Superalloy By Severe Plastic Deformation - Mechanical Machining Case. *Acta Materialia* 180:2–14.
[11] Wang B, Liu Z, Cai Y, Luo X, Ma H, Song Q, Xiong Z (2021) Advancements in Material Removal Mechanism and Surface Integrity of High Speed Metal Cutting: A Review. *International Journal of Machine Tools and Manufacture* 166:103744.
[12] Johnson GR, Cook WH (1985) Fracture Characteristics of Three Metals Subjected to Various Strains, Strain Rates, Temperatures and Pressures. *Engineering Fracture Mechanics* 21(1):31–48.
[13] Xia J, Ding W, Qiu B, Xu J (2020) 3d Simulation Study on the Chip Formation Process in High Speed and Ultra-High Speed Grinding of Nickel-Based Super Alloy. *Diamond & Abrasives Engineering* 40(6):58–69.
[14] Sun C, Hong Y, Xiu S, Yao Y (2021) Grain Refinement Mechanism of Metamorphic Layers by Abrasive Grinding Hardening. *Journal of Manufacturing Processes* 69:125–141.
[15] Zhou J (2013) *Numerical Modeling of Ductile Fracture*, The University of Akron. PhD Dissertation.
[16] Sakai T, Belyakov A, Kaibyshev R, Miura H, Jonas JJ (2014) Dynamic and Post-Dynamic Recrystallization Under Hot, Cold and Severe Plastic Deformation Conditions. *Progress in Materials Science* 60:130–207.